236 (2024) 212763

Contents lists available at ScienceDirect

Geoenergy Science and Engineering

journal homepage: www.sciencedirect.com/journal/geoenergy-science-and-engineering

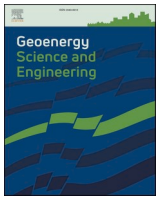

Prediction of thermal front movement in geothermal reservoirs containing distributed natural fractures

Kozo Sato [a,*], Abbas Firoozabadi [b,c]

[a] The University of Tokyo, Frontier Research Center for Energy and Resources, 7-3-1 Hongo Bunkyo-ku, Tokyo, 113-8656, Japan
[b] Rice University, Chemical and Biomolecular Engineering Department, Houston, TX, 77005, USA
[c] Reservoir Engineering Research Institute, 595 Lytton Avenue, Suite B, Palo Alto, CA, 94301, USA

ARTICLE INFO

Keywords:
Fractured geothermal reservoirs
Reinjection
Premature breakthrough
CVBEM
GAM

ABSTRACT

When designing a reinjection scheme for geothermal development, one needs to predict the flow and thermal behavior between the recharge and discharge wells. Premature thermal front breakthrough is of great concern and is often observed in real fields. However, prediction methods based on homogeneous media are prone to overly optimistic estimates. In this study, geothermal reservoirs with vertical fractures which are discretely distributed in the permeable rock are considered, and the streamline simulation is developed and applied to evaluate the thermal front movement, represented by the characteristic times t_D^*. With 1000 simulation results for stochastically generated natural fracture systems, regression models are developed for the expected values of t_D^* with minimal information requirements on fracture parameters. In general, the fracture orientation θ_f has a stronger negative correlation with t_D^* than the total fracture length Σ_f. The intensity of natural fractures has opposing effects (delay or advance) on t_D^* depending on θ_f, and taking this effect into account improves the quality of the regression model. In addition, when the pressure difference between the doublet wells is available, the model accuracy is further improved by incorporating pressure data into the regression. The prediction models are of practical use for understanding the thermal behavior and designing a reinjection scheme in fractured geothermal reservoirs.

1. Introduction

Geothermal energy has been considered as one of the promising energy resources due to its large reserves, low carbon footprint, and non-intermittent deliverability. Heat extraction can be enhanced, and the lifetime of geothermal resources can be extended by continuous reinjection of produced water back into the producing reservoir (Bödvarsson and Tsang, 1982; Gringarten, 1978; Mahmoodpour et al., 2022; Stefansson, 1997), which maintains the reservoir pressure and also meets environmental requirements for fluid disposal. The reinjected water is much colder than the geothermal formation, and reinjection results in cooling around the recharge (injection) well. Such a cooled area expands with time, and eventually, the cold water front reaches the discharge (production) well. The potential risk of reinjection is the premature breakthrough of the cold thermal front to the discharge well, which significantly degrades the efficiency of heat extraction (Li et al., 2016). A sound design should prevent early cold front breakthrough.

Theoretical studies are well established (Gringarten and Sauty, 1975; Lauwerier, 1955; Schulz, 1987; Stopa and Wojnarowski, 2006) for the thermal front movement in homogeneous media. The work of Gringarten and Sauty (1975) is a practical extension of Lauwerier (1955); it has been used to study several geothermal developments (Brun et al., 2011; Satman, 2011; Tsang et al., 1980). Lauwerier (1955) proposed an analytical solution for temperature variation along a linear segment between recharge and discharge wells (doublet wells) with heat loss to confining layers, assuming constant fluid velocity. Gringarten and Sauty (1975) applied the Lauwerier's solution to stream channels between doublet wells, along which the fluid velocity is expressed as a function of the stream channel area from the recharge well. The semi-analytical model can simulate thermal behavior in homogeneous media with heat exchange from surrounding rocks and is applicable to different well arrangements, including doublet wells.

In geothermal fields, premature cold front breakthrough is often observed (Fadel et al., 2022; Pruess and Bodvarsson, 1984), and the models based on the assumption of homogeneous media end up with overly optimistic estimates. The thermal front movement is highly

* Corresponding author.
E-mail address: kozo@g.ecc.u-tokyo.ac.jp (K. Sato).

https://doi.org/10.1016/j.geoen.2024.212763
Received 31 July 2023; Received in revised form 3 March 2024; Accepted 6 March 2024
Available online 12 March 2024

dependent on geothermal field geology (Bödvarsson and Tsang, 1982). Most geothermal fields are heterogeneous and naturally fractured, and prediction of thermal front movement requires consideration of preferential flow paths due to fractures. Bödvarsson and Tsang (1982) considered a geothermal reservoir containing equally spaced horizontal fractures that are completely penetrated by a recharge well. Owing to symmetry, only one sector consisting of a single fracture is modeled, where radial flow within a horizontal fracture between impermeable rock is examined. Pruess and Bodvarsson (1984) considered a more drastic path between recharge and discharge wells; that is, one-dimensional linear flow through a vertical fracture embedded in impermeable rock, and investigated thermal interference along a preferential flow path.

The geological setting of interest in this study is geothermal reservoirs with vertical fractures discretely distributed within permeable rock, which describes many geothermal fields (Boersma et al., 2021; Fadel et al., 2022; Glaas et al., 2021; Mahmoodpour et al., 2022). For fractured reservoirs, idealized approaches are often used, such as dual-porosity modelling (Kazemi et al., 1976; Warren and Root, 1963) and permeability anisotropy (Durlofsky, 1991; Pickup et al., 1994). These approaches assume that fracture heterogeneity may be simplified to macroscopic homogeneity, which is reasonable for a diffusive (equalization) process, such as pressure behavior. Thermal front movement, however, is a process of differentiation rather than equalization, and the idealized approaches may overlook the true influence of natural fractures on the thermal front movement. Indeed, when applied to geothermal development, the permeability anisotropy approach (Dussel et al., 2016) does not properly model the premature breakthrough (Fadel et al., 2022).

The complex variable boundary element method (CVBEM) has been developed to accurately model discretely distributed fracture systems and verified by simulating fluid displacement behavior (Sato and Abbaszadeh, 1996) and evaluating the equivalent permeability tensor (Nakashima et al., 2000). The approach has been used to study the effect of discrete fractures on isothermal tracer flow (Sato and Abbaszadeh, 1996), horizontal well productivity (Sato, 1997, 2000), drained rock volume between fractured wells (Khanal and Weijermars, 2019), and sweep patterns in water flooding (Weijermars et al., 2020). Unlike idealized approaches, the CVBEM accounts for the geometric characteristics of individual discrete fractures and provides accurate and realistic fluid movement through fractured reservoirs. In this study, the technique proposed by Gringarten and Sauty (1975), which is applicable to a homogeneous medium, is implemented in the CVBEM to simulate the thermal front movement in fractured media.

In the early stages of geothermal field development, detailed fracture characterization may not be available, and deterministic modelling of flow and thermal behavior in fractured media may not be described properly. The need for simple and inexpensive means to study reinjection in fractured geothermal reservoirs prompted us to develop easy-to-use prediction models with minimal information requirements on fracture parameters. For this purpose, numerical experiments are performed with the above-mentioned simulator in order to collect data on the thermal front movement in stochastically generated fracture systems. The simulation results are analysed by using a nonparametric regression technique to uncover the relationship between response and predictor variables. The prediction model developed in this study is of practical use for understanding thermal behavior and designing a reinjection scheme in fractured geothermal reservoirs.

2. Method of solution

2.1. Streamline tracking through fractured media

For an incompressible and irrotational fluid flow of pressure p and viscosity μ through a horizontal homogeneous porous medium of permeability k and porosity φ, the complex potential:

$$\Omega = \Phi + \mathrm{i}\Psi \tag{1}$$

satisfies the Laplace equation

$$\nabla^2\Omega = 0 \tag{2}$$

where Φ is the velocity potential, defined as $\Phi = (k/\mu)p$, and Ψ is the stream function. The Cauchy's integral formula for the complex potential Ω, analytic inside and along a simple closed boundary Γ, is

$$\Omega(z) = \frac{1}{2\pi\mathrm{i}}\oint_{\Gamma}\frac{\Omega(\zeta)}{\zeta - z}\mathrm{d}\zeta \tag{3}$$

where ζ is on Γ and the contour integral is calculated by traversing so that the domain of interest lies on the left. This formula states that the values of Ω interior to Γ are completely determined by knowing the values of Ω on Γ. Since there may be no analytical evaluation of the contour integral in Eq. (3), the boundary Γ is divided into boundary elements and the integral is approximated as a summation of line integrals along the elements; the numerical procedure is known as the CVBEM (Sato, 2015).

When there exist singularities, such as point sources/sinks (wells) and line objects (fractures), in the flow domain, the complete numerical solution $\widetilde{\Omega}(z)$ is obtained by use of superposition. In the CVBEM, $\widetilde{\Omega}(z)$ is given as the sum of the non-singular solution $\widetilde{\Omega}^{\mathrm{ns}}(z)$, which is the numerical approximation of Eq. (3), and the singular solutions for wells $\Omega_{\mathrm{w}j}(z)$ and fractures $\Omega_{\mathrm{f}l}(z)$:

$$\widetilde{\Omega}(z) = \widetilde{\Omega}^{\mathrm{ns}}(z) + \sum_{j=1}^{n_{\mathrm{w}}}\Omega_{\mathrm{w}j}(z) + \sum_{l=1}^{n_{\mathrm{f}}}\Omega_{\mathrm{f}l}(z) \tag{4}$$

where n_{w} is the number of wells and n_{f} is the number of natural fractures. The singular solution $\Omega_{\mathrm{w}j}(z)$ for the well j located at $z_{\mathrm{w}j}$ is given by

$$\Omega_{\mathrm{w}j}(z) = -\frac{q_{\mathrm{w}j}}{2\pi h}\ln\left(z - z_{\mathrm{w}j}\right) \tag{5}$$

where $q_{\mathrm{w}j}$ is the injection rate and h is the formation thickness. For the fracture l given by the line segment from z_1 to z_2 in the physical z plane, its singular solution $\Omega_{\mathrm{f}l}(\chi)$ in the mapped χ plane is given by (Sato, 2015)

$$\Omega_{\mathrm{f}l}(\chi) = \sum_{n=1}^{m_{\mathrm{L}}}\frac{a_{-n}}{\chi^n} + \sum_{j=1}^{m_{\mathrm{p}}}\left(\frac{\beta_j\chi_{\mathrm{p}j}}{\chi - \chi_{\mathrm{p}j}} + \frac{\overline{\beta_j\chi_{\mathrm{p}j}}}{\chi - \overline{\chi_{\mathrm{p}j}}}\right) \tag{6}$$

where the first expansion is the Laurent series of order m_{L} about the origin and the remaining expansions are the first-order Laurent series about m_{p} complex conjugate pairs of poles located at $\chi_{\mathrm{p}j}$ and $\overline{\chi_{\mathrm{p}j}}$ (Fig. A. 1). The coordinate χ is defined by the inverse Joukowski transformation in terms of z_1 and z_2. The unknown coefficients a_{-n} and β_j are to be determined by the conditions given in Appendix A.

The CVBEM is used for tracking streamlines, as they are the level curves of the stream function and Eq. (4) yields the stream function as its imaginary part. Let z_j be a point on a certain streamline, which has a stream function of Ψ_0, then the next point z_{j+1} can be found by solving the equation

$$\Psi(z) - \Psi_0 = 0 \tag{7}$$

for z. The time increment $\Delta\tau_j$ required for the fluid particle to move from z_j to z_{j+1} is obtained as

$$\Delta\tau_j = \frac{\Delta r_j}{v_j} = \varphi\frac{2\left|z_{j+1} - z_j\right|}{\left|W_{j+1} + W_j\right|} \tag{8}$$

where the distance $\Delta r_j = \left|z_{j+1} - z_j\right|$ is divided by the average interstitial velocity over the interval, $v_j = \left|W_{j+1} + W_j\right|/(2\varphi)$ with the definition of complex velocity: $W = -\mathrm{d}\Omega/\mathrm{d}z$.

Numerical procedures for the CVBEM, including detailed treatment of singularities and streamline tracking schemes, are described in Sato (2015).

2.2. Temperature along streamlines

Gringarten and Sauty (1975) considered heat extraction from geothermal reservoirs with continuous reinjection. The dimensionless temperature T_D along a streamline connecting the recharge and discharge wells is defined as

$$T_D = \frac{T_0 - T(S, t_D)}{T_0 - T_i} \tag{9}$$

where T_0 is the initial temperature of the geothermal reservoir, T_i the temperature of the injected water and $T(S, t_D)$ the temperature when the stream-channel area is S and at time t_D. T_D of 0 indicates the initial condition and T_D of 1 implies that the reservoir is completely cooled to the temperature of the injected water. The dimensionless time t_D is defined as

$$t_D = \frac{\rho_w C_w}{\rho_a C_a} \frac{qt}{d^2 h} \tag{10}$$

where $\rho_w C_w$ is the volumetric heat capacity of water, $\rho_a C_a$ the volumetric heat capacity of the geothermal rock, q the flow rate, h the reservoir thickness, and d the characteristic length.

Let us introduce the concept of time of flight (TOF) τ, defined as

$$\tau \equiv \int_0^s \frac{dr}{|v(r)|} \tag{11}$$

where s is the arc length along the streamline corresponding to S and $v(r)$ is the interstitial velocity at r. Using the dimensionless TOF, defined as $\tau_D = q\tau/(d^2 h)$, the solution for T_D, given by Eq. (7) in Gringarten and Sauty (1975), is rewritten (simplified) as

$$T_D = \operatorname{erfc}\left[\frac{\tau_D}{\sqrt{\lambda(t_D - \tau_D)}}\right] \tag{12}$$

where λ is the heat exchange coefficient between the reservoir and surrounding rocks, defined as

$$\lambda = \frac{\rho_w C_w \rho_a C_a}{K_r \rho_r C_r} \frac{qh}{d^2} \tag{13}$$

where $\rho_r C_r$ is the volumetric heat capacity and K_r the thermal conductivity of surrounding rocks. When $\lambda \geq 10^4$, the heat transfer between the reservoir and surrounding rocks is negligible (Gringarten and Sauty, 1975), while $\lambda = 0$ indicates infinite heat transfer. The dimensionless temperature of the produced water T_{wD} at the discharge well is obtained by integrating Eq. (12) with respect to the dimensionless stream function $\psi = \Psi h/q$ as

$$T_{wD} = \int_0^1 \operatorname{erfc}\left[\frac{\tau_{wD}}{\sqrt{\lambda(t_D - \tau_{wD})}}\right] d\psi \tag{14}$$

where τ_{wD} is the dimensionless TOF at the discharge well.

The analytical solution, Eq. (12), was derived for steady state flow under simplifying assumptions (Gringarten and Sauty, 1975). In terms of fluid properties, the volumetric heat capacity and viscosity are assumed to be constant; the contrast in properties between the injected (cold) and in-situ (hot) water is neglected. These properties are temperature dependent. In Appendix B discussion on temperature dependency will be presented.

2.3. Streamline simulation

In the CVBEM, a sufficient number of streamlines are tracked to characterize the detailed flow in the domain of interest. At every tracking point z_j, the velocity v_j can be evaluated, and the TOF is approximated as

$$\tau \equiv \int_0^s \frac{dr}{|v(r)|} \approx \sum_{j=0}^{m} \Delta\tau_j \tag{15}$$

where $\Delta\tau_j$ is given by Eq. (8) and m is the number of tracking from 0 to s. For individual streamlines, the dimensionless temperature T_D at arc length s and time t_D is calculated by using Eqs. (12) and (15). With n_s streamlines tracked from the recharge well to the discharge well, T_{wD} given by Eq. (14) is numerically approximated as

$$T_{wD} = \sum_{i=1}^{n_s} \operatorname{erfc}\left[\frac{\tau_{wDi}}{\sqrt{\lambda(t_D - \tau_{wDi})}}\right] \Delta\psi_i \tag{16}$$

where τ_{wDi} and $\Delta\psi_i$ are τ_{wD} and the increment of ψ along the i-th streamline, respectively.

2.3.1. Application to homogeneous media

In this study, boundary effects are assumed to be negligible, and the boundary Γ in the CVBEM is set far enough away to have no effect on the results. From the recharge well at $(0, -0.5)$ to the discharge well at $(0, 0.5)$ in a homogeneous medium, streamlines are tracked by using the CVBEM. The initial 360 tracking points are allocated evenly along the well circumference from $r_w \exp(-0.4\pi i)$ to $r_w \exp(1.4\pi i)$ with $r_w = 10^{-4}$. Fig. 1 (a) shows the tracked streamlines. Tracking is normally terminated when the streamline reaches the discharge well. In addition, if the tracking point deviates to $y < -1$ or $|x| > 1$, it is forced to terminate because such a streamline would take too long to reach the discharge well and does not affect the result during the time period of interest.

In a homogeneous medium, the breakthrough of the displacing fluid (water) occurs at $t_D = \pi/3$ (Gringarten, 1978). Fig. 1 (b), (c), and (d) show the T_D distributions at $t_D = \pi/3$ for $\lambda = 10^4$, 10, and 1,

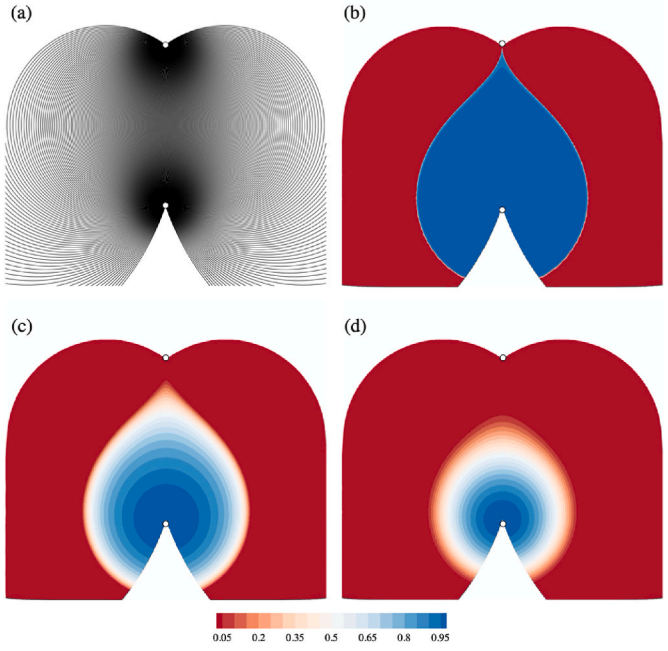

Fig. 1. Streamline simulation for a homogeneous medium: (a) Streamlines, and dimensionless temperature T_D distributions at $t_D = \pi/3$ for three values of heat exchange coefficient (b) $\lambda = 10^4$, (c) $\lambda = 10$, and (d) $\lambda = 1$.

respectively. When the heat transfer is negligible ($\lambda = 10^4$), the thermal front is identical to the displacing front, which is sharp and not smeared, as shown in Fig. 1 (b). A clear cusp towards the discharge well is observed at breakthrough. In condition of moderate heat transfer ($\lambda = 10$), the thermal front becomes smeared towards the upstream side, as shown in Fig. 1 (c). Consequently, the thermal breakthrough is slightly delayed, and the cooled area shrinks. These observations become more pronounced for strong heat transfer ($\lambda = 1$), as shown in Fig. 1 (d). Behind the thermal front, the dimensionless temperature T_D becomes lower as λ decreases due to the heat supply from the surrounding rocks.

Fig. 2 shows the dimensionless temperature at the discharge well T_{wD} evaluated by Eq. (16) for different values of λ from 0.3 to 10^5. When the heat exchange with the surrounding rocks is negligible ($\lambda \geq 10^4$), thermal breakthrough occurs at $t_D = 1.047$, which is consistent with the analytical solution of $\pi/3$. As the heat exchange increases (λ decreases), breakthrough occurs at later times: $t_D = 1.090$ for $\lambda = 10$ and $t_D = 1.388$ for $\lambda = 1$. In addition to the delay of the breakthrough, the subsequent T_{wD} profiles are low for small values of λ. This implies that heat extraction continues after the thermal breakthrough. For example, at $t_D = 3$, T_{wD} for $\lambda = 1$ is as small as 0.07 and the temperature of the produced water is still close to the initial temperature of the geothermal reservoir, while T_{wD} for $\lambda = 10^4$ is 0.48, around the average temperature of the injected water and the geothermal reservoir.

3. Numerical experiments

3.1. Distributed natural fractures

For the numerical experiments, 1000 realizations with different combinations of fracture parameters are prepared in a $1\times$ 1 square domain between the dipole wells. As basic fracture parameters within the domain of interest, the fracture orientation (θ_f), the total fracture length (Σ_f), the number of fractures (n_f), and the geometric mean of fracture lengths (m_f) are considered under the assumption of log-normal fracture length distributions. The orientation θ_f is defined with respect to the x-axis and drawn from a uniform distribution $U(0, \pi/2)$. The total length Σ_f is drawn from a uniform distribution $U(1, 20)$, and the geometric mean m_f is independently drawn from $U(0.01, 0.2)$. Then, Σ_f is randomly decomposed into the number of fractures n_f (≤ 100) and individual fracture lengths a_f according to the log normal distribution. Fig. 3 shows the scatter plot of these fracture parameters.

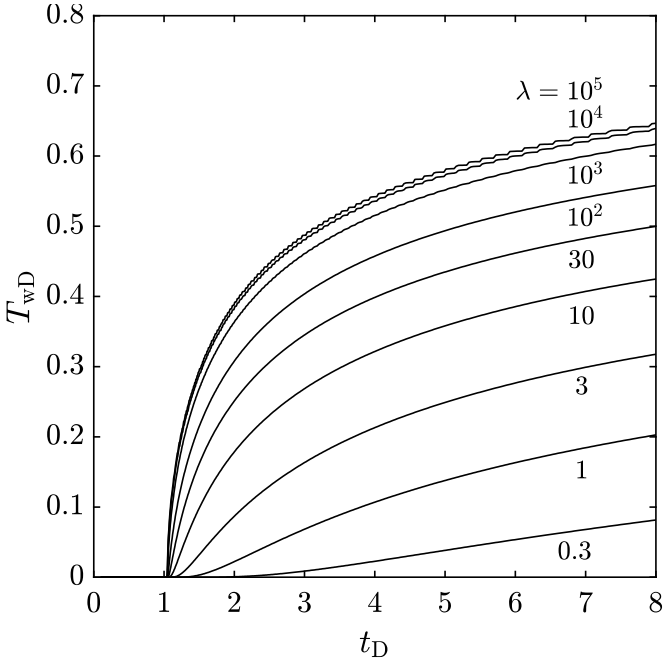

Fig. 2. Dimensionless temperature T_{wD} at the discharge well in a homogeneous medium for heat exchange coefficient λ from 0.3 to 10^5.

Individual fracture images are generated by an unconditional Boolean technique, which randomly distributes n_f fractures of length a_f in space. Sample realizations for the Σ_f–θ_f pairs, marked in color in Fig. 3, are shown in Fig. 4, and the corresponding fracture parameters are listed in Table 1. Fractures are assumed to be unidirectional in this work. The underlying assumption is that the contrast between the maximum and minimum horizontal stresses is large, so that only fractures parallel to the maximum stress direction have a significant effect on flow.

3.2. Simulation for sample realizations

3.2.1. Streamline tracking

In the CVBEM, fractures are modeled by the singular solution given by Eq. (6) with $m_L = 5$ and $m_p = 5$. The fracture conductivity $k_f w_f$ in Eq. (A. 1) is set high enough to be practically infinite, which corresponds to macrofractures (van Golf-Racht, 1982). Fig. 5 shows the streamlines tracked from the recharge well at $(0, -0.5)$ through the fractured media A, B, C, and D to the discharge well at $(0, 0.5)$. The fractures are distributed in a limited region of the 1×1 domain, and the model results are accurate as long as the heat extraction of interest is limited within the region.

Fig. 5 (A) shows the streamlines through a moderately fractured system ($\Sigma_f = 9.87$) almost parallel to the well alignment ($\theta_f = 1.563$). Compared with Fig. 1 (a), the streamline profile between the doublet wells is strongly distorted. Due to the high $k_f w_f$, the velocity potential along each fracture is almost constant, and the streamlines are approximately perpendicular to the fractures. As the fracture distribution is mostly symmetric with respect to the well alignment, the streamlines are not strongly deflected in one direction. For the fracture system with similar intensity of natural fractures ($\Sigma_f = 10.29$) but different fracture orientation ($\theta_f = 0.763$), the streamlines tend to deviate according to the fracture orientation, as shown in Fig. 5 (B). This tendency becomes more pronounced when the natural fractures are intense ($\Sigma_f = 19.50$), as shown in Fig. 5 (C). On the contrary, when the fractures are distributed almost perpendicular to the well alignment ($\theta_f = 0.011$), the streamline profile is not much different from that in a homogeneous medium. In particular, the natural fractures in the middle between the doublet wells do not have much effect on the flow profile, as shown in Fig. 5 (D). These fractures almost coincide with the equi-potential lines for a homogeneous case.

3.2.2. Temperature at discharge well

Fig. 6 shows the dimensionless temperatures T_{wD} at the discharge well for the fractured media compared with T_{wD} for a homogeneous medium for $\lambda = 10^4$, 10, and 1. When heat transfer is negligible ($\lambda = 10^4$), T_{wD} increases rapidly after the thermal breakthrough as seen in Fig. 6 (left), which implies that further heat extraction is limited. The breakthrough time $t_D|_{BT}$ is a key element of geothermal development with low heat transfer. In addition, $t_D|_{BT}$ can also be used as a pessimistic estimate of the thermal breakthrough time when the intensity of heat transfer is unknown, since $t_D|_{BT}$ is the earliest time at which heat extraction can deteriorate drastically. On the contrary, when the heat transfer is indeed strong ($\lambda = 1$), the increase in T_{wD} after breakthrough is gradual, as observed in Fig. 6 (right). Due to prolonged heat extraction, after twice the breakthrough time, the temperature drop of the produced water is still less than 10% ($T_{wD} = 0.1$). The lifetime of geothermal development is expected to be long, and the time when T_{wD} becomes 0.1 ($t_D|_{T_{wD}=0.1}$) is chosen as the time of interest for $\lambda = 1$. For moderate heat transfer ($\lambda = 10$), T_{wD} increases moderately, as shown in Fig. 6 (middle), which may restrict the development lifetime. The time when T_{wD} becomes 0.3 ($t_D|_{T_{wD}=0.3}$) is chosen as the critical time for $\lambda = 10$.

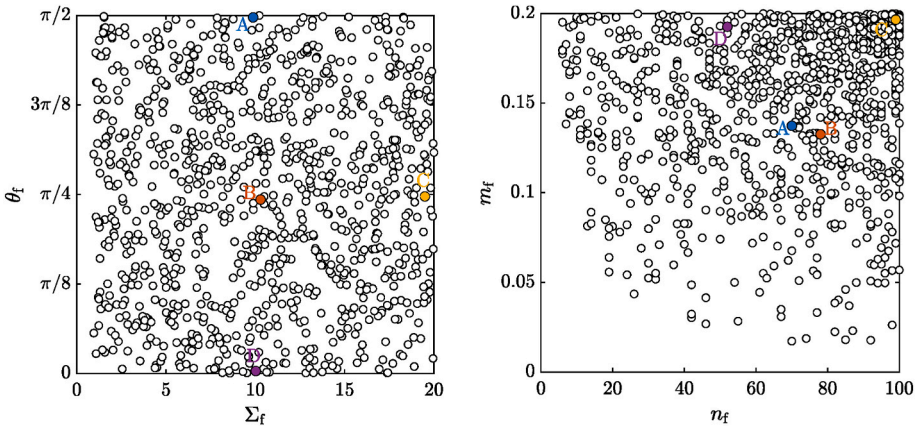

Fig. 3. Numerical experiment settings: fracture orientation θ_f and total fracture length Σ_f (left) and geometric mean of fracture lengths m_f and number of fractures n_f (right).

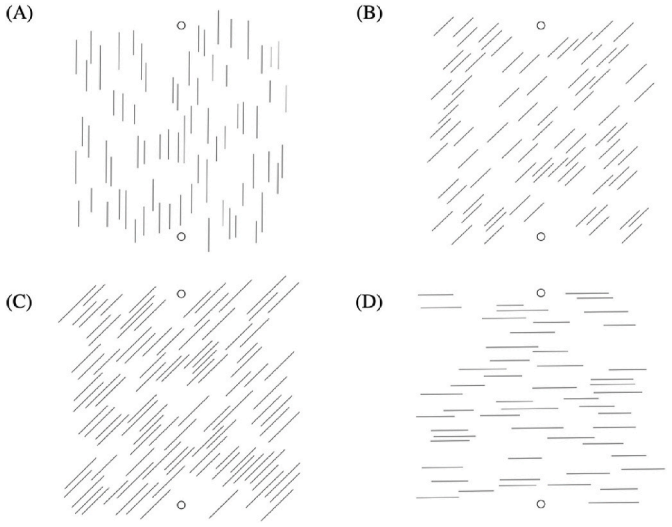

Fig. 4. Sample realizations of fractures: (A) $\theta_f = 1.563$ and $\Sigma_f = 9.87$, (B) $\theta_f = 0.763$ and $\Sigma_f = 10.29$, (C) $\theta_f = 0.777$ and $\Sigma_f = 19.50$, and (D) $\theta_f = 0.011$ and $\Sigma_f = 10.02$.

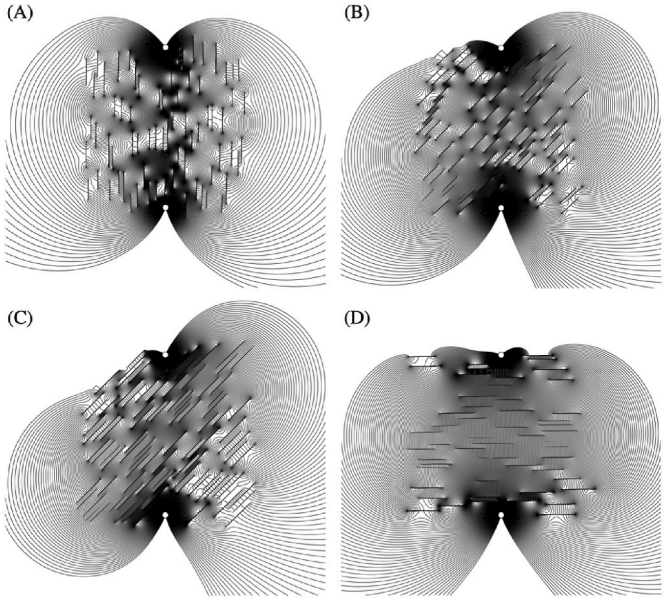

Fig. 5. Streamlines for the fractured media A, B, C, and D. Sample realizations A, B, C, and D are presented in Fig. 4.

Table 1
Fracture parameters of sample realizations and characteristic times for fractured and homogeneous media.

Fracture parameter	A	B	C	D	Homogeneous
θ_f	1.563	0.763	0.777	0.011	–
Σ_f	9.87	10.29	19.50	10.02	–
Characteristic time					
$t_D\|_{BT}$	0.293	0.846	0.871	1.396	1.047
(years)	(22)	(64)	(66)	(106)	(80)
$t_D\|_{T_{wD}=0.3}$	1.488	2.754	2.358	4.074	3.548
(years)	(113)	(209)	(179)	(310)	(270)
$t_D\|_{T_{wD}=0.1}$	1.084	3.217	2.934	5.218	3.824
(years)	(82)	(245)	(223)	(397)	(291)

Table 1 summarizes the dimensionless characteristic times t_D^*; $t_D|_{BT}$ for $\lambda = 10^4$, $t_D|_{T_{wD}=0.3}$ for $\lambda = 10$, and $t_D|_{T_{wD}=0.1}$ for $\lambda = 1$, for the fractured media A, B, C, and D compared with those for a homogeneous medium. For parameters of $q = 100$ m^3/h, $h = 100$ m, $\rho_w C_w / \rho_a C_a = 1.5$, and $d = 1,000$ m (the distance between the wells), Eq. (10) gives $t = 6.7 \times 10^5 t_D$ (hrs). Then, for a homogeneous medium, the characteristic times $t^* = 80$, 270, and 291 years for $\lambda = 10^4$, 10, and 1, respectively. These t^* values vary from 22 to 106 years, 113–310 years, and 82–397 years, respectively, for the sample fractured media.

Fig. 7 shows t^* in years for the fractured media and the relative scales to the homogeneous case. Regardless of the value of λ, the fractured medium A yields much smaller t^* and the medium D yields larger t^* than those for a homogeneous medium. The difference in t^* can be more than 100 years, suggesting that the effect of natural fractures on geothermal development is quite large. The fractured medium B, which has the same intensity of natural fractures (Σ_f) as the media A and D, yields t^* in between. The obvious feature that distinguishes these three fractured media A, B, and D is the fracture orientation θ_f, as seen in Fig. 3 (left). The fractured medium C, which is oriented similarly to (but more densely fractured than) the medium B, yields t^* values that are not much different from those of the medium B. These observations imply that the fracture orientation θ_f is the dominant controlling factor of the characteristic times.

3.2.3. Spatial variation of temperature

To understand the differences in the characteristic times for different fracture systems, one may examine the spatial variation of the temperature T_D within the flow domain. Fig. 8 shows the T_D distributions at thermal breakthrough in the fractured media A, B, C, and D with $\lambda =$

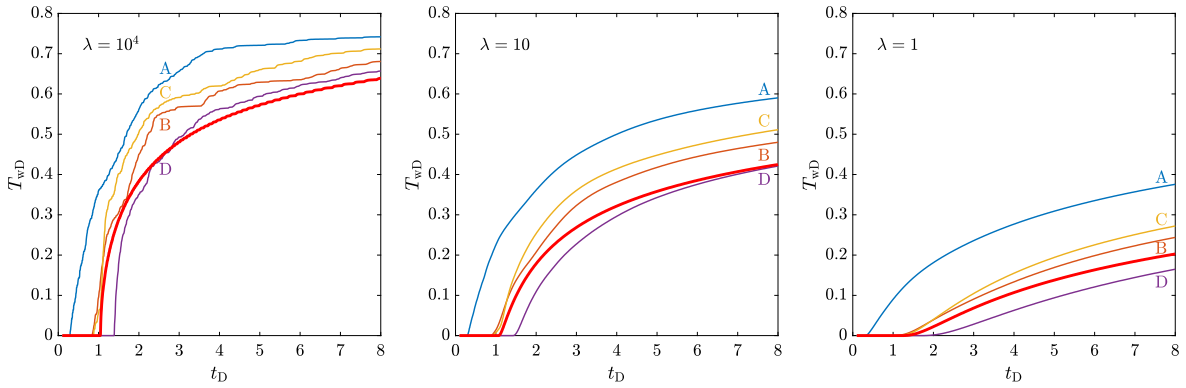

Fig. 6. Dimensionless temperature T_{wD} at the discharge well in the fractured media A, B, C, and D (presented in Fig. 4) compared with T_{wD} in a homogeneous medium (red) with heat exchange coefficient $\lambda = 10^4$ (left), $\lambda = 10$ (middle), and $\lambda = 1$ (right).

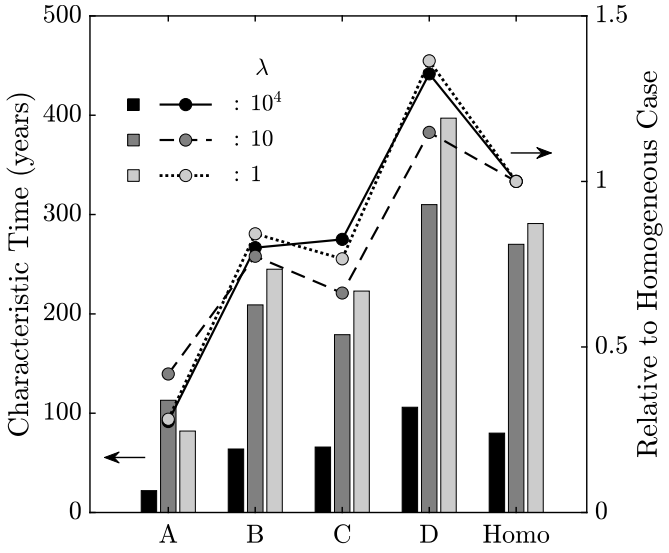

Fig. 7. Characteristic times for fractured and homogeneous media.

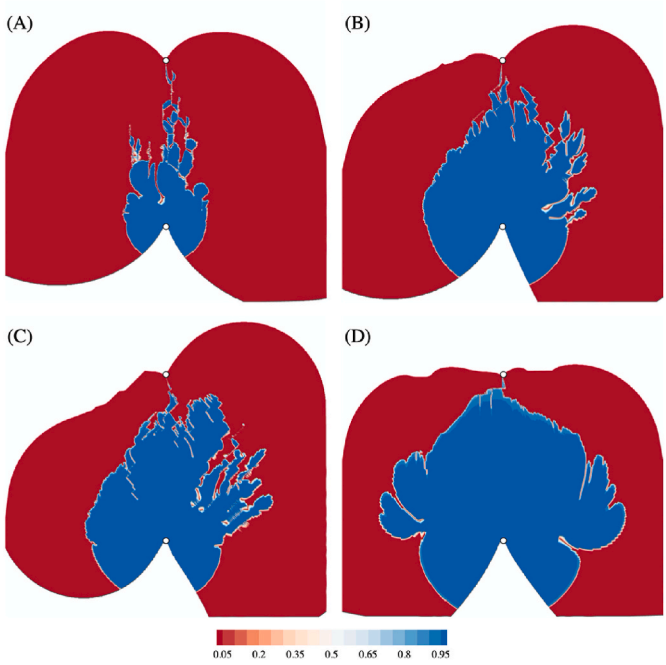

Fig. 8. Dimensionless temperature T_D distributions at thermal breakthrough in the fractured media A, B, C, and D (presented in Fig. 4) with heat exchange coefficient $\lambda = 10^4$.

10^4. Comparison with the homogeneous case shown in Fig. 1 (b) reveals the influence of natural fractures on the T_D distribution. In the fractured medium A ($\theta_f = 1.563$), owing to the preferential flow paths developed between the doublet wells, a much earlier breakthrough ($t_D|_{BT} = 0.293 < \pi/3$) occurs, resulting in a smaller area swept (cooled) by the injected water, as shown in Fig. 8 (A). In contrast, in the fractured medium D, the natural fractures lead the displacing fluid towards the fracture orientation ($\theta_f = 0.011$) and enlarge the cooled area at late breakthrough ($t_D|_{BT} = 1.396 > \pi/3$), as shown in Fig. 8 (D). When the fracture orientation is in between, around $\theta_f = \pi/4$, as shown in Fig. 8 (B) and (C), the cooled area is also in the middle of the two fracture cases A and D and is rather close to the homogeneous case.

Fig. 9 shows the T_D distributions for $T_{wD} = 0.3$ in the fractured media with $\lambda = 10$. Compared with the case of $\lambda = 10^4$, the thermal front becomes smeared due to the moderate heat supply from the surrounding rocks. The characteristic times are longer than those in the previous case (Table 1 and Fig. 7), which means that more water has been injected. The cooled areas in Fig. 9, where T_D is greater than 0, are enlarged, indicating that larger areas are contacted by the injected water. The enlargement of the cooled area, however, is not proportional to the increase in t_D^*. For instance, in the fractured medium D, t_D^* for $\lambda = 10$ ($t_D|_{T_{wD}=0.3} = 4.074$) is almost three times higher than for $\lambda = 10^4$ ($t_D|_{BT} = 1.396$), indicating that three times as much water is injected. The cooled area in Fig. 9 (D) is not expanded as much, compared with Fig. 8 (D). This indicates that the heat supply of $\lambda = 10$ is effective in maintaining the temperature of the geothermal reservoir at a certain level.

Fig. 10 shows the T_D distributions for $T_{wD} = 0.1$ in the fractured media with $\lambda = 1$. Compared with the previous two cases of $\lambda = 10^4$ and $\lambda = 10$, the thermal front becomes further smeared due to the strong heat supply from the surrounding rocks. Except for the medium A, the characteristic times are longer than in the previous case of $\lambda = 10$ (Table 1 and Fig. 7). Although more water has been injected, the cooled areas in Fig. 10, indicated by T_D greater than 0, are respectively smaller than those in Fig. 9. This is because the strong heat supply ($\lambda = 1$) from the surrounding rocks during this time period is sufficient to keep the temperature of the geothermal reservoir high.

3.3. Simulation for stochastic fracture systems

For the 1000 realizations of natural fractures presented in 3.1, the CVBEM is applied to collect data of the thermal front movement. Fig. 11 shows the T_{wD} profiles for the fractured media, compared with T_{wD} for a homogeneous medium. Only 100 simulation results are shown in this

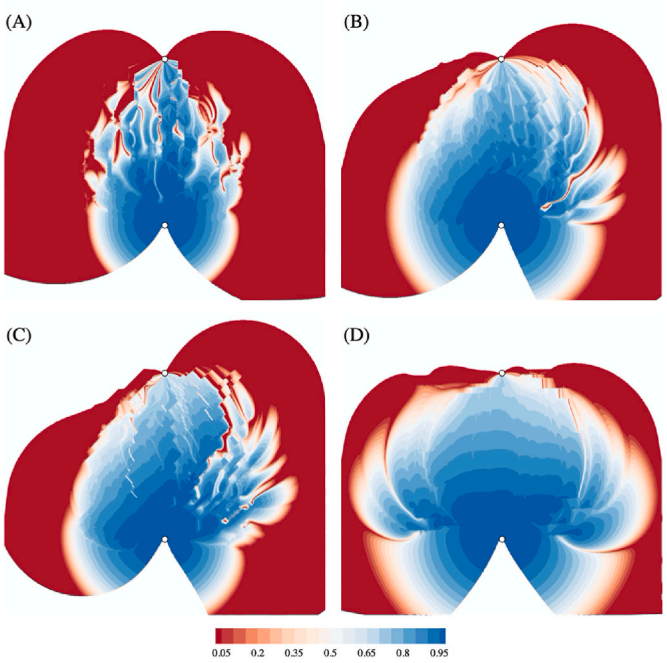

Fig. 9. Dimensionless temperature T_D distributions for $T_{wD} = 0.3$ in the fractured media A, B, C, and D (presented in Fig. 4) with heat exchange coefficient $\lambda = 10$.

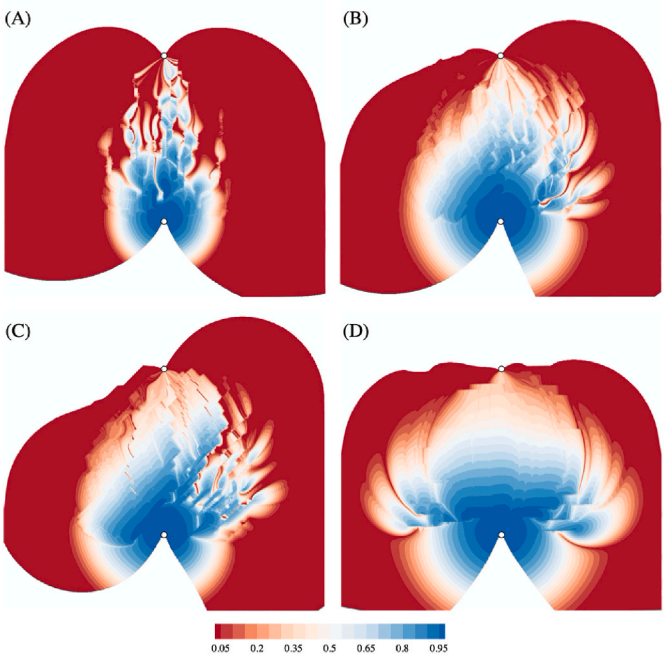

Fig. 10. Dimensionless temperature T_D distributions for $T_{wD} = 0.1$ in the fractured media A, B, C, and D (presented in Fig. 4) with heat exchange coefficient $\lambda = 1$.

figure for clarity, and a full set of 1000 results is used in the subsequent analysis. In all λ cases, the simulation results at early times (around thermal breakthrough times) are distributed around the profile for a homogeneous medium. As time passes (t_D increases), the T_{wD} profiles tend to be shifted above the profile for a homogeneous medium, and eventually all results are above the homogeneous case, as seen in Fig. 11 (left) and (middle). Natural fractures can be favorable or unfavorable for heat extraction in early stages, while they tend to be unfavorable in later stages.

Natural fractures also affect the dimensionless pressure difference Δp_D between the doublet wells. In a homogeneous medium, Δp_D for a doublet system is obtained analytically as (Sato, 2015)

$$\Delta p_D = \frac{1}{\pi} \ln \frac{d}{r_w} \tag{17}$$

which yields $\Delta p_D = 2.932$ for $d/r_w = 10^4$. Natural fractures increase the apparent permeability of the flow domain, and Δp_D decreases, which is advantageous for geothermal development operations. Fig. 12 shows the cross-plot of the characteristic times t_D^* and Δp_D for the 1000 simulations. As expected, the simulated values of Δp_D are always lower than the maximum value of $\Delta p_D = 2.932$ and can take small values below 2.5, which corresponds to a 15% reduction of Δp_D.

When the doublet wells are aligned (sub-)parallel to the natural fractures (θ_f close to $\pi/2$), shown by the yellowish markers in Fig. 12, the characteristic times decrease from the corresponding values of the homogeneous case; from 1.047 to 0.1311, 3.548 to 0.7371, and 3.824 to 0.4677 for $\lambda = 10^4$, 10, and 1, respectively. In contrast, when the wells are aligned nearly perpendicular to the fractures (θ_f close to 0), indicated by the purplish markers in Fig. 12, the characteristic times respectively increase from the corresponding values of the homogeneous case; from 1.047 to 1.594, 3.548 to 4.315, and 3.824 to 6.166 for $\lambda = 10^4$, 10, and 1. It is interesting that the fracture systems exhibit opposing effects (delay or advance) on t_D^* depending on the fracture orientation θ_f. This is also confirmed in Fig. 13, the cross-plot of t_D^* and θ_f. Within a range of relatively small values of θ_f, the characteristic times t_D^* tend to increase in accordance with the intensity of natural fractures (increasing Σ_f); the lighter markers are above the darker ones. The opposite is true for relatively large values of θ_f. The characteristic times tend to decrease with increasing Σ_f; the lighter markers are below the darker makers. While the natural fractures (sub-)parallel to the well alignment are advantageous in lowering the pressure difference Δp_D, they are disadvantageous in shortening the characteristic times t_D^*.

4. Prediction of characteristic times

Based on the numerical experiment results, the prediction of characteristic times with simple predictor variables can be prepared. There is often no prior information about the functional forms relating response variables to possible predictor variables. This difficulty can be alleviated by data-driven approaches that build on the regression model by allowing the shapes of the relationships between response and covariate variables to be learned from the data. In general, model flexibility (usually equivalent to accuracy) and interpretability tend to conflict. In this study, the relationship between the thermal front movement and the fracture parameters is of interest, and both inference (relying on interpretability) and prediction (with high accuracy) are important perspectives. In this context, the generalized additive model (GAM) (Hastie and Tibshirani, 1990; Wood, 2017) provides a compromise that addresses the trade-off between flexibility and interpretability (Zschech et al., 2022).

4.1. General additive model

To uncover nonlinear covariate effects of possible predictor variables X_j on the response variable Y, the GAM assumes additivity of the predictor effects and postulates a regression model as

$$E(Y) = \alpha + \sum_{j=1}^{n_p} f_j(X_j) \tag{18}$$

where $E(Y)$ is the expected value of Y, n_p the number of predictor variables, α the bias term, and f_j the smooth functions. The unknown functions f_j are estimated from the data using scatterplot smoothers,

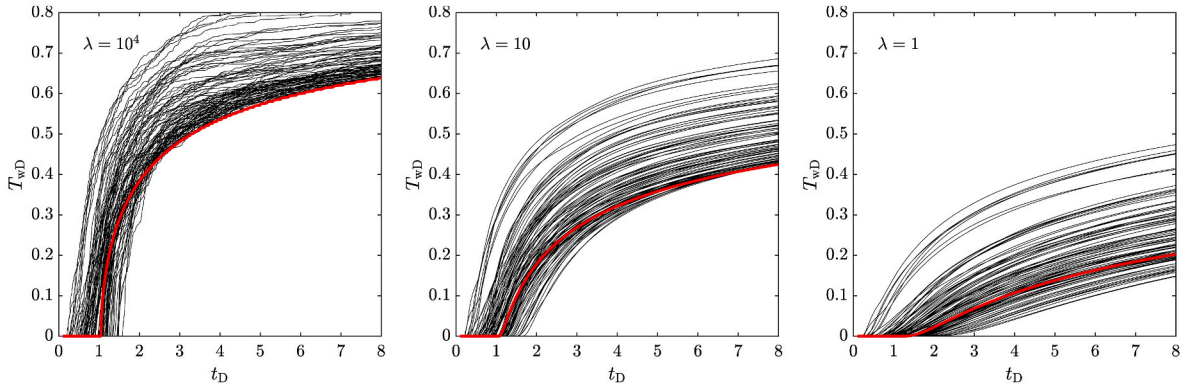

Fig. 11. Dimensionless temperature T_{wD} at the discharge well: 100 simulation results in the stochastic fractured media (black) compared with T_{wD} in a homogeneous medium (red) for heat exchange coefficient $\lambda = 10^4$ (left), $\lambda = 10$ (middle), and $\lambda = 1$ (right).

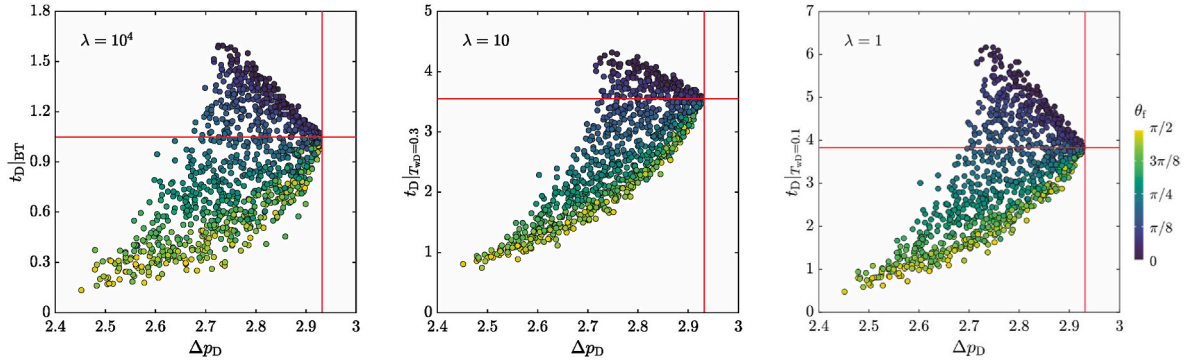

Fig. 12. Characteristic times and Δp_D for heat exchange coefficient $\lambda = 10^4$ (left), $\lambda = 10$ (middle), and $\lambda = 1$ (right). The corresponding values of t_D and Δp_D for a homogeneous medium are indicated by red lines.

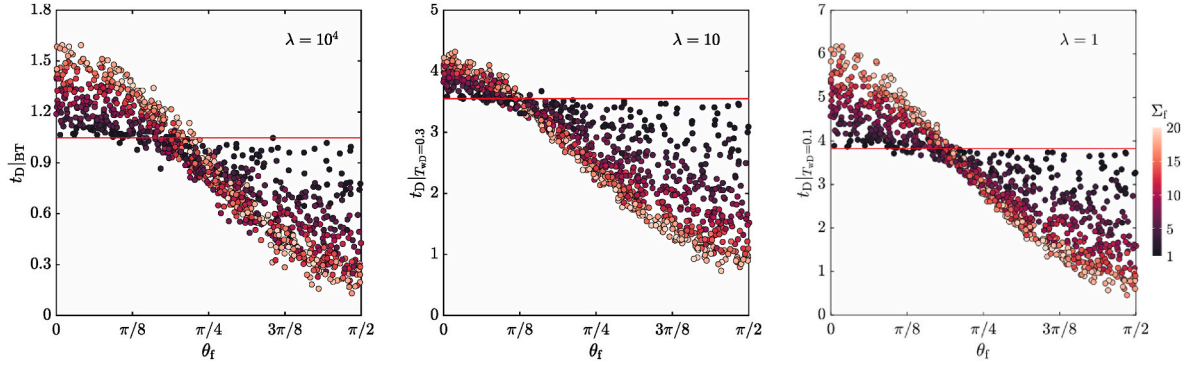

Fig. 13. Characteristic times and θ_f for heat exchange coefficient $\lambda = 10^4$ (left), $\lambda = 10$ (middle), and $\lambda = 1$ (right). The corresponding values of t_D for a homogeneous medium are indicated by red lines.

such as local regression, smoothing splines, and regression splines. In this study, thin plate splines (Wood, 2017), which are classified as regression splines, are employed to fit individual smooth functions. With regression splines, each smooth function f_j can be represented as a linear combination of a finite set of basis functions $b_{j,k}(X_j)$ multiplied by the corresponding coefficients $\beta_{j,k}$:

$$f_j(X_j) = \sum_{k=1}^{n_q} \beta_{j,k} b_{j,k}(X_j) \tag{19}$$

where n_q is the basis size that determines the complexity of each smooth function.

The coefficients $\beta_{j,k}$ are determined so that the log-likelihood of the model (L) is maximized. A large basis size yields a higher likelihood, whereas it could also lead to overfitting, which makes the smooth function wigglier rather than smoother. To avoid overfitting, a smoothing penalty that influences the basis function coefficients is introduced to prevent excessive wiggliness of each smooth function. The wiggliness is represented by $\boldsymbol{\beta}^T \boldsymbol{S} \boldsymbol{\beta}$, where $\boldsymbol{\beta}$ is the parameter vector and $\boldsymbol{S}$ is the penalty matrix specific to the form of the basis functions. Thus, the penalized log-likelihood used for determining the coefficients $\beta_{j,k}$ is defined as $L - \widehat{\lambda} \boldsymbol{\beta}^T \boldsymbol{S} \boldsymbol{\beta}$, where $\widehat{\lambda}$ is the smoothing parameter that controls a trade-off between data fitting and smoothness. If $\widehat{\lambda}$ is set equal to zero, the penalty has no effect and the model yields an interpolating spline; on the other hand, if $\widehat{\lambda}$ is infinite, the penalty removes all basis functions,

resulting in a straight line. As an objective selection method of $\widehat{\lambda}$, the restricted maximum likelihood (REML) criterion (Wood, 2017) is used in this study.

4.2. Regression model I

As a basic prediction model for the characteristic time t_D^*, the first regression model (Model I) is defined with the fracture orientation (θ_f) and the total fracture length (Σ_f) as the predictor variables:

$$E(t_D^*) = \alpha + f_\theta(\theta_f) + f_\Sigma(\Sigma_f) \tag{20}$$

The number of fractures (n_f) and the geometric mean of the fracture lengths (m_f) can be used instead of Σ_f. The accuracy of the regression model improves with more detailed fracture parameters. In contrast, the versatility of the model decreases as the variable becomes more descriptive. In the present case, using n_f and m_f instead of Σ_f yields only a minor improvement, and θ_f and Σ_f are chosen as adequate predictor variables between accuracy and versatility.

Fig. 14 (top two) shows the partial effects f_θ and f_Σ of the respective predictor variables θ_f and Σ_f estimated by the GAM. In all t_D^* cases, the fracture orientation θ_f has a stronger effect on t_D^* than the total fracture length Σ_f. This is in agreement with the observation in 3.2. The partial effect f_θ decreases as θ_f increases from 0 to $\pi/2$, indicating that t_D^* becomes smaller as more fractures become parallel to the path between the doublet wells. In addition, the slope of f_θ is not constant; there are gently sloping segments at each end ($\theta_f \le \pi/8$ and $3\,\pi/8 \le \theta_f$) with a steeper sloping segment ($\pi/8 \le \theta_f \le 3\pi/8$) in between, that is, θ_f has relatively strong effects on t_D^* when $\pi/8 \le \theta_f \le 3\pi/8$.

The bias values α are listed in Table 2. Given the fracture parameters θ_f and Σ_f, the response variable t_D^* can be predicted by Eq. (20) with α, f_θ, and f_Σ, as demonstrated in Appendix C. The predictions are compared with the actual characteristic times in Fig. 14 (bottom). The residual sum of squares (RSS) is listed in Table 2 along with the adjusted R-squared (R^2), a high value of which indicates that the model properly describes the variability in the response variable (Wood, 2017).

The cross-plots of the response variables shown in Fig. 14 (bottom) reveal that the prediction quality of Model I is not satisfactory. The prediction results can be divided into two distinct clusters: over-predictions of t_D^* for smaller values of Σ_f, indicated by the darker markers, and under-predictions of t_D^* for larger values of Σ_f, indicated by the lighter markers. This defect can be inferred from the interaction of θ_f and Σ_f on t_D^* observed in 3.3 (Figs. 12 and 13). The intensity of natural fractures (Σ_f) has opposing effects on t_D^* depending on θ_f. The regression model defined by Eq. (20) does not separate the opposing partial effects

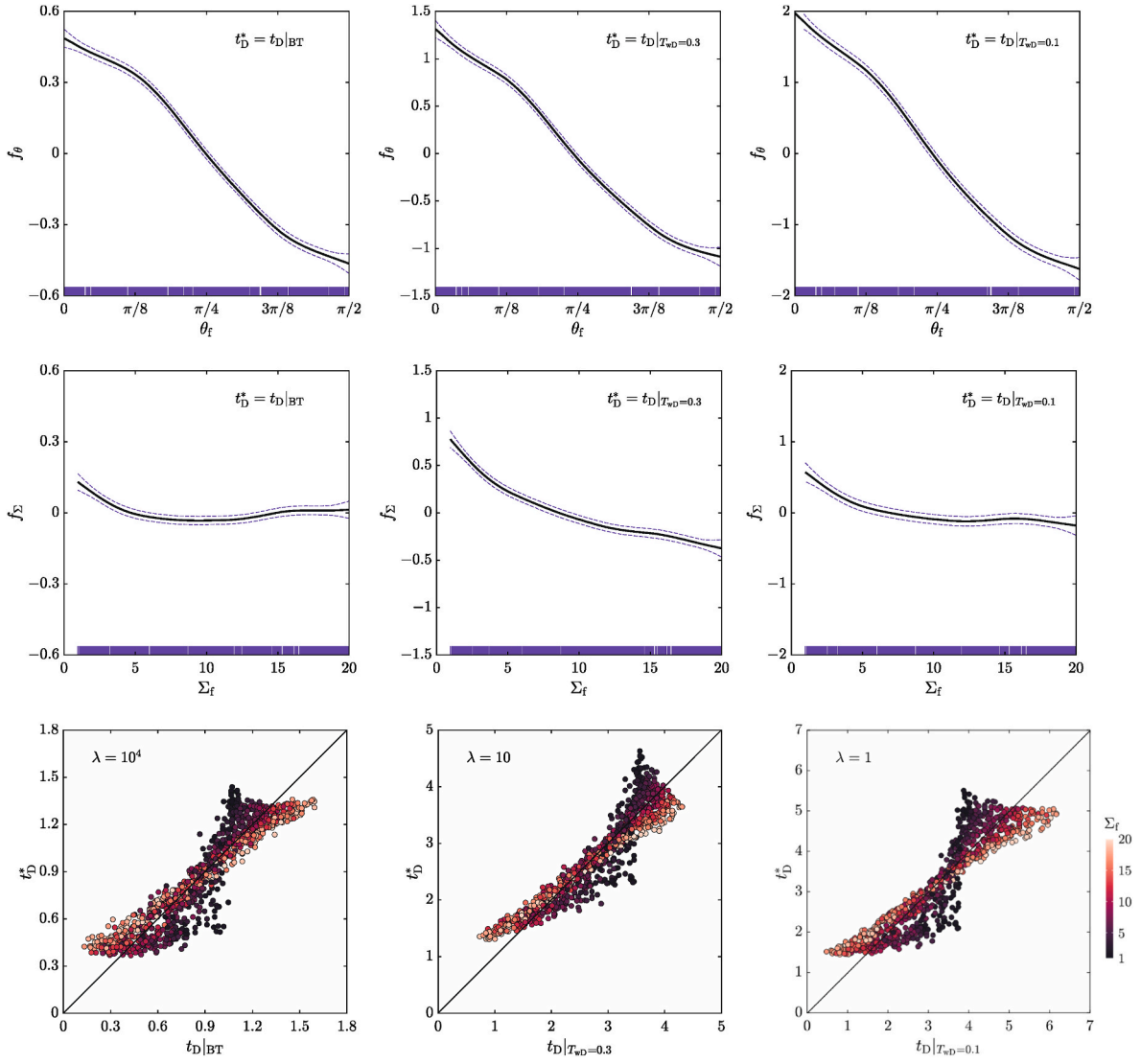

Fig. 14. Partial effects f_θ and f_Σ with 95% confidence intervals (top two) and cross-plots of response variables (bottom) by Model I: $t_D^* = t_D|_{BT}$ (left column), $t_D^* = t_D|_{T_{wD}=0.3}$ (middle column), and $t_D^* = t_D|_{T_{wD}=0.1}$ (right column). Rug plots of 1000 data points appear along the x-axis of f_θ and f_Σ plots.

Table 2
GAM results for Models I, II, and III.

t_D^*		Model I	Model II		Model III	
			(A : $\theta_f < \pi/5$)	(B : $\pi/5 \le \theta_f$)	(A : $\theta_f < \pi/5$)	(B : $\pi/5 \le \theta_f$)
$t_D\|_{BT}$	α	0.864	1.212	0.637	1.212	0.637
	RSS	16.81	7.71		4.93	
	R^2	0.858	0.862	0.791	0.889	0.872
$t_D\|_{T_{wD}=0.3}$	α	2.712	3.564	2.155	3.564	2.155
	RSS	96.83	36.36		14.41	
	R^2	0.875	0.792	0.894	0.809	0.974
$t_D\|_{T_{wD}=0.1}$	α	3.196	4.476	2.361	4.476	2.361
	RSS	258.2	85.27		41.72	
	R^2	0.841	0.835	0.854	0.858	0.949

of Σ_f.

4.3. Regression model II

In the second regression model (Model II), the data set is split into two and the additive model Eq. (20) is applied to each data set individually so that the opposing effects of Σ_f could be properly reflected in each regression model. After preliminary regression trials, the entire set of 1000 simulation data is divided into two groups with a threshold value of $\theta_f = \pi/5$: a data set consisting of 395 data points for $0 \le \theta_f \le \pi/5$ (Data A) and another set of 605 data points for $\pi/5 < \theta_f \le \pi/2$ (Data B).

Fig. 15 (top two) shows the partial effects f_θ and f_Σ of the respective predictor variables θ_f and Σ_f. As in Model I, the partial effect f_θ decreases

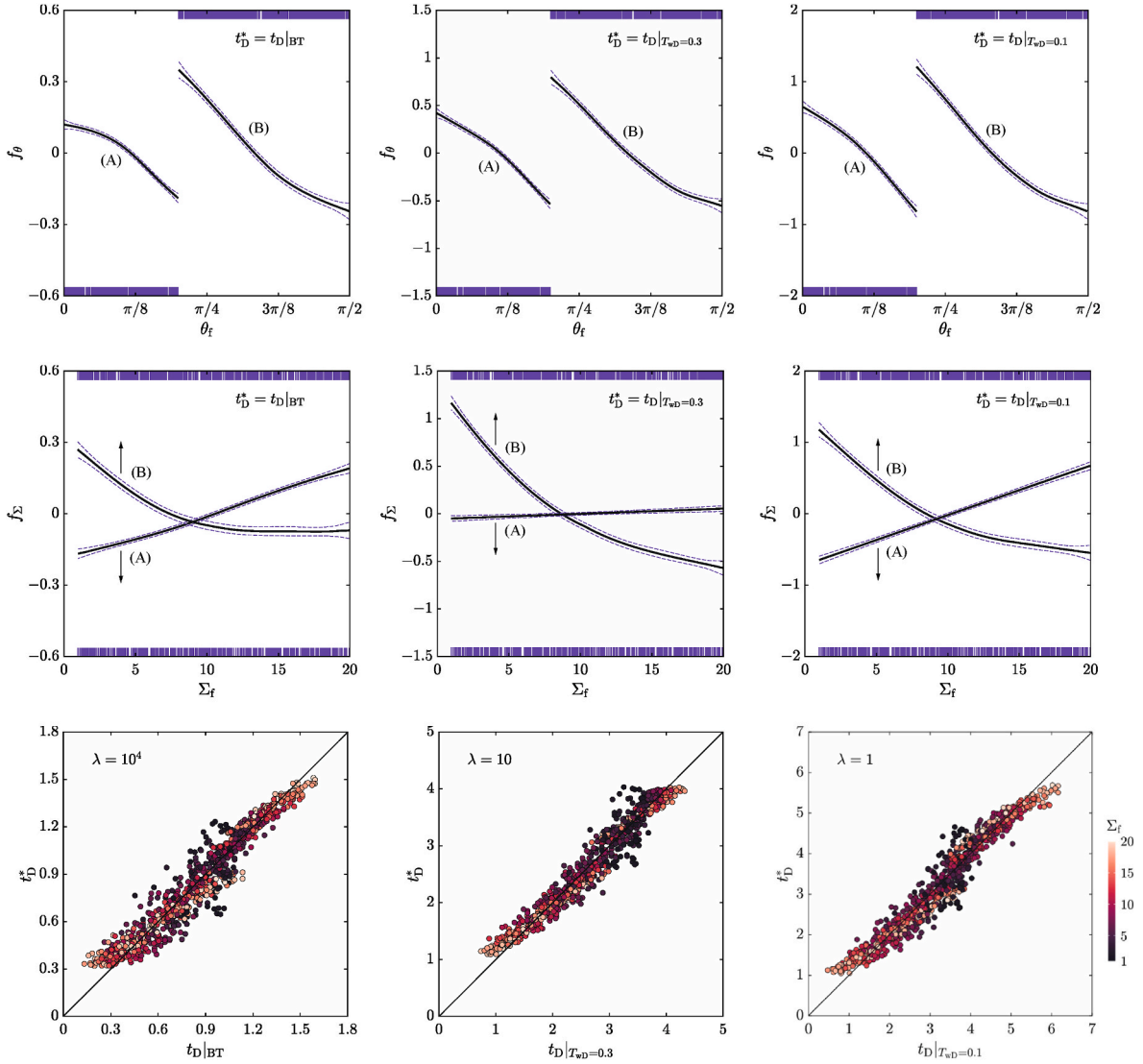

Fig. 15. Partial effects f_θ and f_Σ with 95% confidence intervals (top two) and cross-plots of response variables (bottom) by Model II: $t_D^* = t_D|_{BT}$ (left column), $t_D^* = t_D|_{T_{wD}=0.3}$ (middle column), and $t_D^* = t_D|_{T_{wD}=0.1}$ (right column). Rug plots of 395 data points (Data A) for $0 \le \theta_f \le \pi/5$ appear along the x-axis and those of 605 data points (Data B) for $\pi/5 < \theta_f \le \pi/2$ along the upper x-axis of f_θ and f_Σ plots.

as θ_f increases, and θ_f has a relatively strong effect on t_D^* when $\pi/8 \le \theta_f \le 3\pi/8$. The partial effect f_Σ shows opposite characteristics for two split data sets: increasing f_Σ with Σ_f for Data A and decreasing f_Σ with Σ_f for Data B. The profile of the partial effect f_Σ of Model I (Fig. 14) can be understood as the combined result of suppressing these opposing characteristics.

The Model II predictions are compared with the actual characteristic times in Fig. 15 (bottom), and the corresponding values of α, RSS, and R^2 are given in Table 2. The distinct clusters observed from Model I (Fig. 14) are less obvious in the results of Model II (Fig. 15). Model II yields a significant decrease in the RSS values and improves prediction quality compared with Model I.

4.4. Regression model III

To further improve the prediction quality of Model II, the addition of

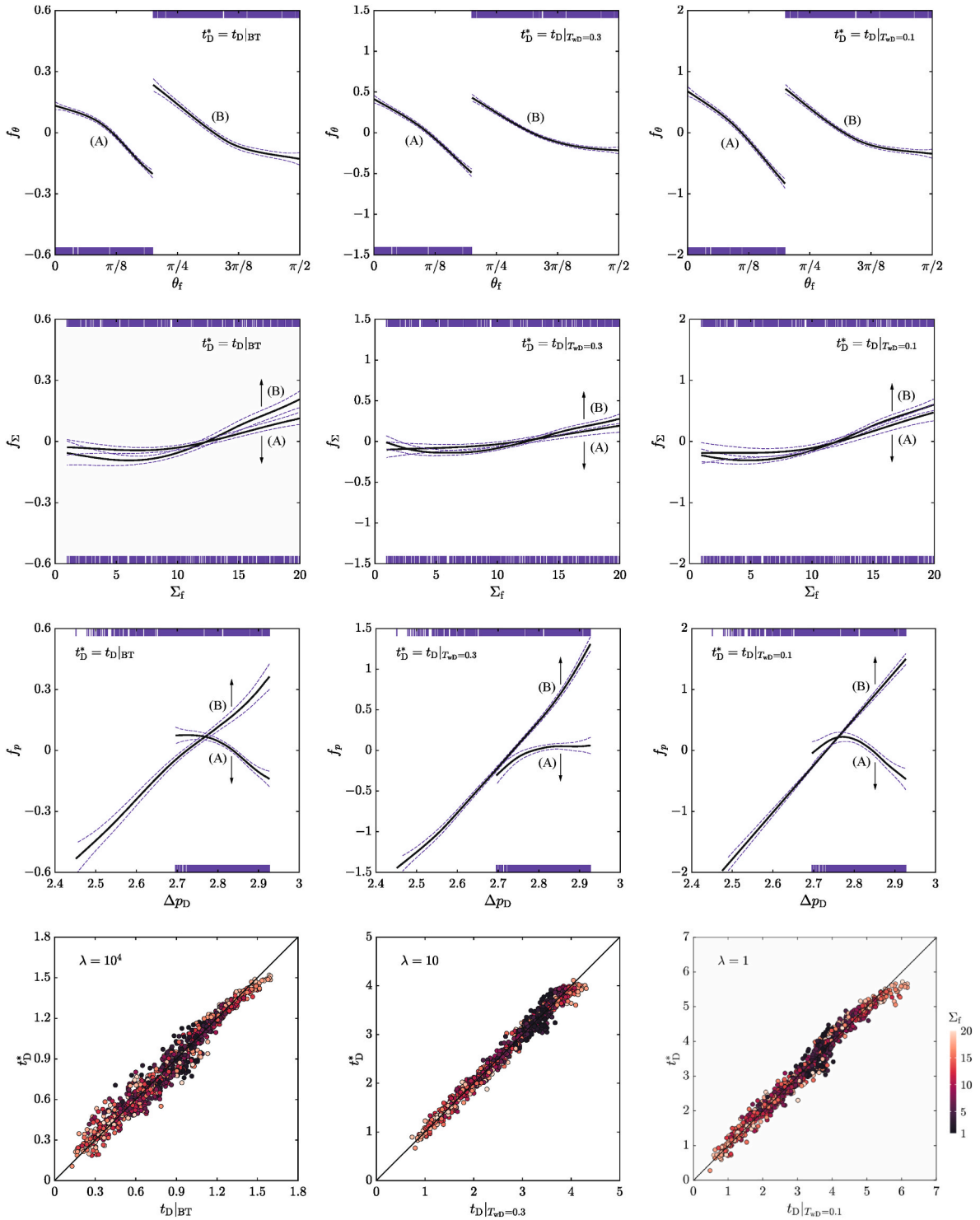

Fig. 16. Partial effects f_θ, f_Σ and f_p with 95% confidence intervals (top three) and cross-plots of response variables (bottom) by Model III: $t_D^* = t_D|_{BT}$ (left column), $t_D^* = t_D|_{T_{wD}=0.3}$ (middle column), and $t_D^* = t_D|_{T_{wD}=0.1}$ (right column). Rug plots of 395 data points (Data A) for $0 \le \theta_f \le \pi/5$ appear along the x-axis and those of 605 data points (Data B) for $\pi/5 < \theta_f \le \pi/2$ along the upper x-axis of f_θ, f_Σ and f_p plots.

a new predictor variable is considered. A potential variable to be included is the pressure difference between the doublet wells Δp_D. In real operations, pressure data are obtained at early stages of development and can be used for operational purposes. The third regression model (Model III) for the response variable t_D^* is defined with the fracture orientation (θ_f), the total fracture length (Σ_f), and the pressure difference (Δp_D) as the predictor variables:

$$E(t_D^*) = \alpha + f_\theta(\theta_f) + f_\Sigma(\Sigma_f) + f_p(\Delta p_D) \tag{21}$$

The additive model Eq. (21) is applied individually to the data sets (Data A and Data B) prepared in the previous section.

Fig. 16 (top three) presents the partial effects f_θ, f_Σ, and f_p of the respective predictor variables θ_f, Σ_f, and Δp_D. The fracture parameters θ_f and Σ_f are static properties that are independent of each other, whereas Δp_D is a dynamic property that is affected by θ_f and Σ_f and is not independent of the fracture parameters. Of the three partial effects, f_p affects t_D^* the most, probably because f_p reflects the effects of θ_f and Σ_f as well as Δp_D. For Data B ($\pi/5 < \theta_f \le \pi/2$), the partial effect f_p is nearly linear to Δp_D, implying that the pressure difference between the doublet wells proportionally affects the characteristic times when the natural fractures are (sub-)parallel to the well alignment. Heat extraction is maintained longer for the doublet wells with larger values of Δp_D. For Data A ($0 \le \theta_f \le \pi/5$), f_p behaves differently depending on λ and Δp_D. In Model III, the relative importance of f_p increases, and the partial effects f_θ and f_Σ become less pronounced in predicting t_D^*. In particular, f_Σ has only a small influence on t_D^* regardless of the data set (Data A or Data B).

The Model III predictions are compared with the actual characteristic times in Fig. 16 (bottom), and the corresponding values of α, RSS, and R^2 are given in Table 2. The outliers observed in the results of Model I and Model II are reduced in the results of Model III. Model III yields a further decrease in the RSS values and improves the prediction quality compared with Model I and Model II.

5. Conclusions

1. The thermal front movement between the doublet wells completed in geothermal reservoirs containing discretely distributed fractures is modeled using the streamline simulation based on the CVBEM coupled with the semi-analytical solution for heat transfer along streamlines.
2. 1000 natural fracture systems are stochastically generated by varying the fracture parameters: the fracture orientation (θ_f) and the total fracture length (Σ_f), with which the streamline simulation is performed to collect data on the thermal front movement, represented by the characteristic times t_D^*.
3. Natural fractures exhibit opposing effects (delay or advance) on t_D^* depending on θ_f. When θ_f is relatively small, the characteristic times t_D^* tend to increase in accordance with the intensity of natural fractures (increasing Σ_f). Conversely, when θ_f is large, the characteristic times tend to decrease with increasing Σ_f.
4. Three kinds of regression models are developed by using the GAM to predict the expected values of t_D^*. Among the fracture parameters used as predictor variables, the fracture orientation θ_f has a stronger effect on t_D^* than the total fracture length Σ_f.
5. In Model I, the GAM with the predictor variables θ_f and Σ_f is applied to the entire set of 1000 data. Since the total fracture length Σ_f has opposing effects on t_D^* depending on θ_f, Model I does not properly separate the opposing partial effects of Σ_f and the prediction quality is not satisfactory.
6. In Model II, the data set is split into two with a threshold value of $\theta_f = \pi/5$, and the GAM with the predictor variables θ_f and Σ_f is applied to each data set individually so that the opposing effects of Σ_f can be properly reflected in each regression model. Model II improves the prediction quality compared with Model I.
7. When the pressure difference Δp_D between the doublet wells is available, Model III uses Δp_D in addition to θ_f and Σ_f as the predictor variables. Model III further improves the prediction quality compared with Model I and Model II.

CRediT authorship contribution statement

Kozo Sato: Conceptualization, Formal analysis, Methodology, Writing – original draft. **Abbas Firoozabadi:** Conceptualization, Methodology, Writing – review & editing.

Declaration of competing interest

The authors declare that they have no known competing financial interests or personal relationships that could have appeared to influence the work reported in this paper.

Data availability

The supplemental data are available in spreadsheet format.

Appendix A. Fracture Singular Solution

Let us consider a fracture with a finite permeability k_f and an aperture w_f with end points z_1 and z_2, as shown in Fig. A. 1 (a). The difference between the values of Ψ on the $-$ and $+$ sides of the fracture at z is equal to the flow rate per unit thickness (q_f/h) inside the fracture:

$$\Psi(z^+) - \Psi(z^-) = \frac{k_f w_f}{k} \frac{d\Phi}{ds}(z) \tag{A. 1}$$

where s is the length measured along the fracture, and Darcy's law is applied to the flow through the fracture. In a geometric sense, w_f is negligibly small, and the values of Φ on the $-$ and $+$ sides of the fracture are equal to each other:

$$\Phi(z^+) - \Phi(z^-) = 0 \tag{A. 2}$$

To derive a singular solution that satisfies Eqs. (A. 1) and (A. 2), the complex potentials on both sides of the fracture must be evaluated. The following two-step conformal mapping is of use to this end:

$$\begin{cases} Z(z) = \dfrac{2z - (z_1 + z_2)}{z_2 - z_1} \\ \chi(Z) = Z + \left(Z^2 - 1\right)^{1/2} \end{cases} \tag{A. 3}$$

The function $Z(z)$ maps the fracture with end points z_1 and z_2 in the z plane onto the line segment from $Z_1 = Z(z_1) = -1$ to $Z_2 = Z(z_2) = 1$, as shown in Fig. A. 1 (b). The function $\chi(Z)$ is the inverse Joukowski transformation that maps the line segment $[-1, 1]$ onto a unit circle $|\chi(Z)| = 1$, as

shown in Fig. A. 1 (c). It follows from the mapping function $\chi(z)$ that points (z^+ and z^-) on opposite sides of the fracture in the z plane are mapped onto points (χ^+ and χ^-) of the unit circle in the χ plane that are each other's complex conjugate.

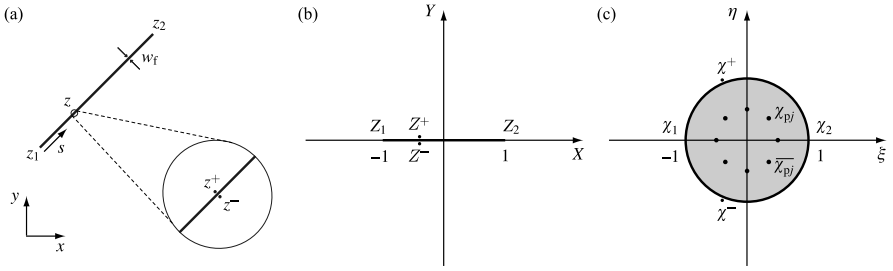

Fig. A. 1. Fracture geometry and mapping: (a) a fracture with end points z_1 and z_2 in the z plane, (b) a line segment $[-1, 1]$ in the Z plane, and (c) a unit circle in the χ plane.

According to Eqs. (A. 1) and (A. 2), the singular solution Ω_f is defined such that its imaginary part Ψ_f is discontinuous and its real part Φ_f is continuous across the fracture and can be chosen such that

$$\Omega_f(\chi) = \overline{\Omega_f(\overline{\chi})} \tag{A. 4}$$

In addition, there should be no influence of Ω_f at ∞:

$$\min_{\chi \to \infty} \Omega_f(\chi) = 0 \tag{A. 5}$$

Since the condition in terms of Ψ given by Eq. (A. 1) is highly problem-specific, one may not generalize a closed-form solution for Eqs. (A. 4) and (A. 5). In such a case, partial sums of Laurent series can be used to derive an approximate solution, which is versatile, as the series coefficients can be determined so that the solution satisfies the individual boundary conditions. The resultant singular solution given by Eq. (6) has the Laurent series about the origin and about the distributed poles located at χ_{pj} and $\overline{\chi_{pj}}$ shown in Fig. A. 1 (c). The former series equally affect the entire boundary of the fracture, while the latter ones individually affect the boundary portion close to the corresponding pole. Hence, the combination of these Laurent series yields a robust representation of both global and local (singular) flow behavior around the fracture (Sato, 2015).

Appendix B. Temperature Dependent Fluid Properties

Fig. B. 1 (left) shows the volumetric heat capacity of water $\rho_w C_w$ at pressures of 30, 40, and 50 MPa and temperatures from 40 °C to 300 °C (Wagner and Pruß, 2002). For a wide range of temperature, $\rho_w C_w$ is fairly stable around 4000 kJ/m^3/K; the assumption that ρC is constant is not strongly violated and seems acceptable for water. On the other hand, the water viscosity μ, shown in Fig. B. 1 (right), varies from 0.66 cP at 40 °C to less than 0.1 cP at 300 °C (Huber et al., 2009). Gringarten and Sauty (1975) discuss the effect of viscosity contrast on thermal front breakthrough by using the analogy of waterflooding and reinjection schemes; thermal breakthrough occurs later when the injected water is more viscous than the in-situ water. In the reinjection scheme, the temperature of the produced water remains at the initial temperature T_0 for a longer period than the breakthrough time $t_D|_{BT}$ evaluated with the analytical solution.

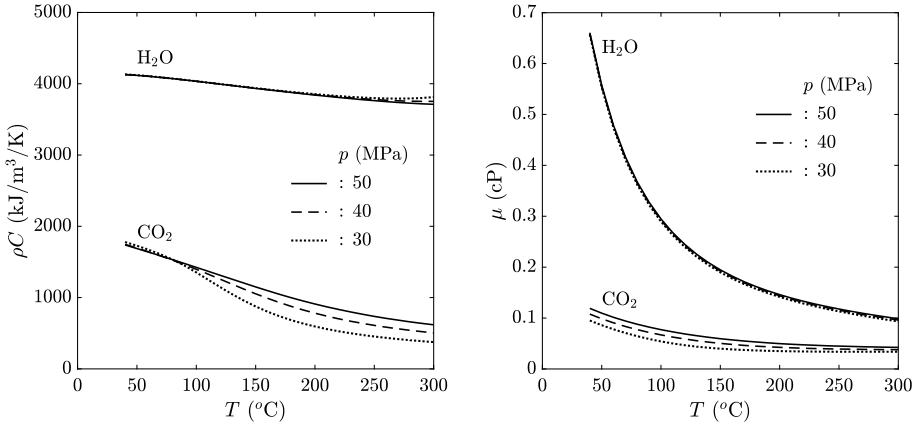

Fig. B. 1. Fluid property dependence on temperature: heat capacities of water and CO_2 (left) and viscosities of water and CO_2 (right) at different pressures.

Fig. B. 1 also shows the relevant properties for carbon dioxide (CO_2) (Laesecke and Muzny, 2017; Span and Wagner, 1996). The use of CO_2 as a heat carrier has attracted much interest in the geothermal industry (Schifflechner et al., 2022) in conjunction with enhanced geothermal systems (EGS) (Pruess, 2006) and carbon capture and storage (CCS) (Randolph and Saar, 2011). Compared to water, the lower heat capacity results in a smaller λ, indicating higher heat transfer between the reservoir and surrounding rocks, and the lower viscosity allows for effective fluid advection. In terms of temperature dependence, the volumetric heat capacity of CO_2 varies from 1750 kJ/m^3/K at 40 °C to less than 620 kJ/m^3/K at 300 °C, and the assumption that ρC is constant is not practically fulfilled. In addition, the CO_2 flow is not in steady state due to the high compressibility of CO_2, and care must be taken when applying the analytical solution for CO_2. The temperature dependence of viscosity is much smaller for CO_2 than for water.

The dimensionless time t_D can be converted to real time t by using Eq. (10), where

$$\frac{\rho_w C_w}{\rho_a C_a} = \frac{\rho_w C_w}{\varphi \rho_w C_w + (1-\varphi)\rho_r C_r} = \left[\varphi + (1-\varphi)\frac{\rho_r C_r}{\rho_w C_w}\right]^{-1} \quad \text{(B. 1)}$$

If the carrier fluid is water and $\rho_w C_w = 4,000$ kJ/m^3/K is used as a representative value for water and $\rho_r C_r = 2,600$ kJ/m^3/K as a typical value for rock, then $\rho_w C_w/\rho_a C_a = 1.5$ for the geothermal reservoir of $\varphi = 0.05$. When the carrier fluid is CO_2, the volumetric heat capacity of CO_2 ($\rho_{CO2} C_{CO2}$) is used for $\rho_w C_w$ in Eq. (B. 1). If $\rho_{CO2} C_{CO2} = 1,000$ kJ/m^3/K, then it follows that $\rho_w C_w/\rho_a C_a = 0.4$. In the conversion of t_D to t, according to Eq. (10), t is inversely proportional to $\rho_w C_w/\rho_a C_a$. Thus, CO_2 as a carrier fluid can increase the characteristic time (or lifetime) by 3.75 (= 1.5 /0.4) times compared to water for the same q.

Appendix C. Prediction Model Usage

Let us use Model II to predict the characteristic times with the predictor variables θ_f and Σ_f. For the sample fracture system D ($\theta_f = 0.011$ and $\Sigma_f = 10.02$) prepared in 3.1, as θ_f is smaller than the threshold value of $\pi/5$, Model II (A) is adopted. For the breakthrough time $t_D|_{BT}$, the bias value $\alpha = 1.212$ is found in Table 2, and the partial effects f_θ at $\theta_f = 0.011$ and f_Σ at $\Sigma_f = 10.02$ are obtained from Fig. 15 (left column). The additive model Eq. (20) yields the estimate of $t_D|_{BT}$ as

$$E(t_D^*) = \alpha + f_\theta(0.011) + f_\Sigma(10.02) = 1.212 + 0.118 - 0.012 = 1.318 \quad \text{(C. 1)}$$

which is close to the actual value of 1.396 (Table 1). For $t_D|_{T_{wD}=0.3}$, $\alpha = 3.564$ from Table 2 and the partial effects f_θ and f_Σ from Fig. 15 (middle column) yields

$$E(t_D^*) = \alpha + f_\theta(0.011) + f_\Sigma(10.02) = 3.564 + 0.411 - 0.001 = 3.974 \quad \text{(C. 2)}$$

For $t_D|_{T_{wD}=0.1}$, $\alpha = 4.476$ from Table 2 and f_θ and f_Σ from Fig. 15 (right column) yields

$$E(t_D^*) = \alpha + f_\theta(0.011) + f_\Sigma(10.02) = 4.476 + 0.631 - 0.018 = 5.089 \quad \text{(C. 3)}$$

The corresponding actual values are 4.074 and 5.218 (Table 1), respectively.

For the sample fracture system B ($\theta_f = 0.763$ and $\Sigma_f = 10.29$), as θ_f is larger than the threshold value of $\pi/5$, Model II (B) is adopted. For the characteristic times $t_D|_{BT}$, $t_D|_{T_{wD}=0.3}$, and $t_D|_{T_{wD}=0.1}$, the bias values $\alpha = 0.637$, 2.155, and 2.361 are respectively found in Table 2, and the partial effects f_θ at $\theta_f = 0.763$ and f_Σ at $\Sigma_f = 10.29$ are obtained from Fig. 15. The resultant estimates are

$$E(t_D^*) = \alpha + f_\theta(0.763) + f_\Sigma(10.29) = 0.637 + 0.245 - 0.052 = 0.830 \quad \text{(C. 4)}$$

for $t_D|_{BT}$,

$$E(t_D^*) = \alpha + f_\theta(0.763) + f_\Sigma(10.29) = 2.155 + 0.556 - 0.134 = 2.577 \quad \text{(C. 5)}$$

for $t_D|_{T_{wD}=0.3}$, and

$$E(t_D^*) = \alpha + f_\theta(0.763) + f_\Sigma(10.29) = 2.361 + 0.830 - 0.168 = 3.023 \quad \text{(C. 6)}$$

for $t_D|_{T_{wD}=0.1}$. The corresponding actual values are 0.846, 2.754, and 3.217 (Table 1), respectively.

The partial effects of Model II (Fig. 15) and Model III (Fig. 16) are available in the supplemental data in spreadsheet format.

Appendix D. Supplementary data

Supplementary data to this article can be found online at https://doi.org/10.1016/j.geoen.2024.212763.

References

Bödvarsson, G.S., Tsang, C.F., 1982. Injection and thermal breakthrough in fractured geothermal reservoirs. J. Geophys. Res. Solid Earth 87 (B2), 1031–1048.

Boersma, Q.D., Bruna, P.O., de Hoop, S., Vinci, F., Moradi Tehrani, A., Bertotti, G., 2021. The impact of natural fractures on heat extraction from tight Triassic sandstones in the West Netherlands Basin: a case study combining well, seismic and numerical data. Neth. J. Geosci. 100, e6.

Brun, M., Hamm, V., Lopez, S., Ungemach, P., Antics, M., Ausseur, J.-Y., Cordier, E., Elodie, G., Goblet, P., Lalos, P., 2011. Hydraulic and thermal impact modelling at the scale of the geothermal heating doublet in the Paris Basin, France. In: Proceedings, Thirty-Sixth Workshop on Geothermal Reservoir Engineering.

Durlofsky, L.J., 1991. Numerical calculation of equivalent grid block permeability tensors for heterogeneous porous media. Water Resour. Res. 27 (5), 699–708.

Dussel, M., Lüschen, E., Thomas, R., Agemar, T., Fritzer, T., Sieblitz, S., Huber, B., Birner, J., Schulz, R., 2016. Forecast for thermal water use from upper jurassic carbonates in the Munich region (south German Molasse basin). Geothermics 60, 13–30.

Fadel, M., Reinecker, J., Bruss, D., Moeck, I., 2022. Causes of a premature thermal breakthrough of a hydrothermal project in Germany. Geothermics 105, 102523.

Glaas, C., Vidal, J., Genter, A., 2021. Structural characterization of naturally fractured geothermal reservoirs in the central Upper Rhine Graben. J. Struct. Geol. 148, 104370.

Gringarten, A.C., 1978. Reservoir lifetime and heat recovery factor in geothermal aquifers used for urban heating. Pure Appl. Geophys. 117, 297–308.

Gringarten, A.C., Sauty, J.P., 1975. A theoretical study of heat extraction from aquifers with uniform regional flow. J. Geophys. Res. 80 (35), 4956–4962.

Hastie, T.J., Tibshirani, R.J., 1990. Generalized Additive Models. Taylor & Francis.

Huber, M.L., Perkins, R.A., Laesecke, A., Friend, D.G., Sengers, J.V., Assael, M.J., Metaxa, I.N., Vogel, E., Mareš, R., Miyagawa, K., 2009. New international formulation for the viscosity of H2O. J. Phys. Chem. Ref. Data 38 (2), 101–125.

Kazemi, H., Merrill Jr., L.S., Porterfield, K.L., Zeman, P.R., 1976. Numerical simulation of water-oil flow in naturally fractured reservoirs. Soc. Petrol. Eng. J. 16 (6), 317–326.

Khanal, A., Weijermars, R., 2019. Pressure depletion and drained rock volume near hydraulically fractured parent and child wells. J. Petrol. Sci. Eng. 172, 607–626.

Laesecke, A., Muzny, C.D., 2017. Reference correlation for the viscosity of carbon dioxide. J. Phys. Chem. Ref. Data 46 (1), 013107.

Lauwerier, H.A., 1955. The transport of heat in an oil layer caused by the injection of hot fluid. Applied Scientific Research, Section A 5 (2), 145–150.
Li, T., Shiozawa, S., McClure, M.W., 2016. Thermal breakthrough calculations to optimize design of a multiple-stage Enhanced Geothermal System. Geothermics 64, 455–465.
Mahmoodpour, S., Singh, M., Bär, K., Sass, I., 2022. Impact of well placement in the fractured geothermal reservoirs based on available discrete fractured system. Geosciences 12 (1), 19.
Nakashima, T., Sato, K., Arihara, N., Yazawa, N., 2000. Effective permeability estimation for simulation of naturally fractured reservoirs. SPE Asia Pacific Oil and Gas Conference and Exhibition.
Pickup, G.E., Ringrose, P.S., Jensen, J.L., Sorbie, K.S., 1994. Permeability tensors for sedimentary structures. Math. Geol. 26 (2), 227–250.
Pruess, K., 2006. Enhanced geothermal systems (EGS) using CO2 as working fluid—a novel approach for generating renewable energy with simultaneous sequestration of carbon. Geothermics 35 (4), 351–367.
Pruess, K., Bodvarsson, G.S., 1984. Thermal effects of reinjection in geothermal reservoirs with major vertical fractures. J. Petrol. Technol. 36 (9), 1567–1578.
Randolph, J.B., Saar, M.O., 2011. Combining geothermal energy capture with geologic carbon dioxide sequestration. Geophys. Res. Lett. 38 (10).
Satman, A., 2011. Sustainability of geothermal doublets. Proceedings, Thirty-Sixth Workshop on Geothermal Reservoir Engineering.
Sato, K., 1997. Productivity of horizontal sinks in the presence of distributed fractures. SPE J. 2 (2), 194–203.
Sato, K., 2000. Productivity correlation for horizontal sinks completed in fractured reservoirs. SPE Reservoir Eval. Eng. 3 (2), 132–138.
Sato, K., 2015. Complex Analysis for Practical Engineering. Springer International Publishing.
Sato, K., Abbaszadeh, M., 1996. Tracer flow and pressure performance of reservoirs containing distributed thin bodies. SPE Form. Eval. 11 (3), 185–193.
Schifflechner, C., Wieland, C., Spliethoff, H., 2022. CO2 plume geothermal (CPG) systems for combined heat and power production: an evaluation of various plant configurations. J. Therm. Sci. 31 (5), 1266–1278.
Schulz, R., 1987. Analytical model calculations for heat exchange in a confined aquifer. J. Geophys. 61 (1), 12–20.
Span, R., Wagner, W., 1996. A new equation of state for carbon dioxide covering the fluid region from the triple-point temperature to 1100 K at pressures up to 800 MPa. J. Phys. Chem. Ref. Data 25 (6), 1509–1596.
Stefansson, V., 1997. Geothermal reinjection experience. Geothermics 26 (1), 99–139.
Stopa, J., Wojnarowski, P., 2006. Analytical model of cold water front movement in a geothermal reservoir. Geothermics 35 (1), 59–69.
Tsang, C.F., Bodvarsson, G.S., Lippmann, M.J., Rivera, R.J., 1980. Some aspects of the response of geothermal reservoirs to brine reinjection with application to the Cerro Prieto field. Geothermics 9 (1), 213–220.
van Golf-Racht, T.D., 1982. Fundamentals of Fractured Reservoir Engineering. Elsevier Scientific Publishing Co., Amsterdam.
Wagner, W., Pruß, A., 2002. The IAPWS formulation 1995 for the thermodynamic properties of ordinary water substance for general and scientific use. J. Phys. Chem. Ref. Data 31 (2), 387–535.
Warren, J.E., Root, P.J., 1963. The behavior of naturally fractured reservoirs. Soc. Petrol. Eng. J. 3 (3), 245–255.
Weijermars, R., Khanal, A., Zuo, L., 2020. Fast models of hydrocarbon migration paths and pressure depletion based on complex analysis methods (CAM): mini-review and verification. Fluids 5 (1), 7.
Wood, S.N., 2017. Generalized Additive Models: an Introduction with R. CRC Press/Taylor & Francis Group.
Zschech, P., Weinzierl, S., Hambauer, N., Zilker, S., Kraus, M., 2022. GAM(e) changer or not? An evaluation of interpretable machine learning models based on additive model constraints, the 30th European Conference on Information Systems (ECIS 2022).